

Title

Quantitative and qualitative evaluation of sequential PET/MRI using a newly developed mobile PET system for brain imaging

Running Head

MR-compatible flexible brain PET

Original Article

Abstract

Purpose: To evaluate the clinical feasibility of newly developed mobile PET system with MR-compatibility (flexible PET; fxPET), compared with conventional PET (cPET) /CT for brain imaging.

Methods: Twenty-one patients underwent cPET/CT with subsequent fxPET/MRI using ^{18}F -FDG. As qualitative evaluation, we visually rated image quality of MR and PET images using four-point scoring system. We evaluated overall image quality for MR, while we evaluated overall image quality, sharpness and lesion contrast. As quantitative evaluation, we compared registration accuracy between two modalities ([fxPET and MRI] and [cPET and CT]) measuring spatial coordinates. We also examined accuracy of regional ^{18}F -FDG uptake.

Results: All acquired images were of diagnostic quality and the number of detected lesions did not differ significantly between fxPET/MR and cPET/CT. Mean misregistration was significantly larger with fxPET/MRI than with cPET/CT. SUVmax and SUVmean for fxPET and cPET showed high correlations in the lesions ($R=0.84, 0.79$; $P<0.001, P=0.002$, respectively). In normal structures, we also showed high correlations of SUVmax ($R=0.85, 0.87$; $P<0.001, P<0.001$, respectively) and SUVmean ($R=0.83, 0.87$; $P<0.001, P<0.001$, respectively) in bilateral caudate nuclei and a moderate correlation of SUVmax ($R=0.65$) and SUVmean ($R=0.63$) in vermis.

Conclusions: The fxPET/MRI system showed image quality within the diagnostic range, registration accuracy below 3mm and regional ^{18}F -FDG uptake highly correlated with that of cPET/CT.

Key words

mobile PET; PET/MRI; PET/CT

Abbreviations

fxPET; flexible PET, cPET; conventional PET, SUV; standardized uptake value

Introduction

PET works the best when combining other modalities such as CT or MRI, for complementing insufficient structural information. PET/CT has been widely used in clinical settings, successfully combining the molecular information from PET with anatomical information from CT [1-5].

PET/MRI has been introduced into clinical practices and PET/MRI shows various advantages, such as excellent soft-tissue contrast, reduced radiation exposure and additional functional information [6-8]. The superior soft-tissue contrast of MRI results in diagnostic advantages, particularly for lesions in the brain, head and neck, heart, liver, pelvis and bone marrow [9-11]. The reduced exposure to radiation also represents a major advantage, peculiarly in pediatric cases and repeated studies for longitudinal follow-up [12, 13]. MRI can provide useful functional information such as diffusion, perfusion and MR spectroscopy [14-16]. PET/MRI is thus expected to be one of the most powerful imaging tools for diagnosis.

However, introducing PET/MRI systems into daily clinical settings is not always easy. Because PET/MRI faces technical challenges such as MR-based attenuation correction (MRAC) and the issue of a small transaxial FOV, in addition to practical limitations including costs and spaces for the installation of new system. One possible

solution to the latter is to introduce a mobile PET system that can be combined with an existing MR unit, achieving an instant PET/MRI system [17].

Here, we introduce a newly developed mobile PET system with MR-compatibility called “flexible PET” (fxPET) (Shimadzu Corporation, Kyoto, Japan). The fxPET scanner consists of a silicon photomultiplier (SiPM)-based depth-of-interaction (DOI) TOF detector [18, 19], attaining high spatial resolution and sufficient FOV of 150 mm in the axial plane. Combining this fxPET system with an existing MR scanner, we can achieve an fxPET/MRI system (Electronic supplementary material 1).

There are concerns exist about the fxPET/MRI system, including registration of both images, incomplete data acquisition and MRAC. As the fxPET is an external-type scanner, sequential acquisition is mandatory. A previous study showed that registration accuracy of PET/MRI was better with simultaneous acquisition than with sequential acquisition outside the brain [20]. We thus need to clarify the registration accuracy of fxPET/MRI in the brain regions. As incomplete data acquisition (due to the open ring form) and MRAC method selection would affect the image quality from fxPET/MRI, evaluation of image quality seems crucial.

As for brain imaging, MRI gives much more information from excellent soft-tissue contrast and various advanced sequences, while CT provides limited structural

information. The combination of PET and MRI thus seems particularly effective for brain imaging.

The purpose of this prospective study was to evaluate the clinical feasibility of the fxPET/MRI for brain imaging, compared with conventional PET (cPET)/CT.

Materials and methods

Patients

Consecutive twenty-one patients (13 females, 8 males; age range 21-77 years; mean, 53 ± 15 years) who were examined for clinical purpose between February 2015 and May 2015 were recruited when fxPET/MRI was available for research scan. Twelve patients had intracranial lesions (glioblastoma, n=3; metastasis, n=2; meningioma, n=2, anaplastic astrocytoma, n=1; schwannoma, n=1; ependymoma, n=1, craniopharyngioma, n=1; old hemorrhage, n=1). The location of the intracranial lesions was as follows: brain parenchyma, n=10, extracranial, n=1; skull, n=1. The remaining nine patients had no visible intracranial lesions, although lesions responsible for symptoms such as epileptic attack were suspected. The current study was done based on the local institutional review board approved "fxPET/non-contrast MRI" study whose purpose was the evaluation of clinical feasibility of fxPET/MRI. Prior to the participation in this study, written informed

consent was obtained from all patients in a manner.

Protocol overview

All patients fasted for at least 4 hours before intravenous ^{18}F -FDG injection, showing a blood glucose concentration below 200 mg/dl just before injection. We injected ^{18}F -FDG at 3.7 MBq/kg body weight and started scanning at 30 minutes after injection. After cPET/CT was performed based on a standard clinical protocol, each patient moved to the fxPET/MRI unit, then fxPET was performed, followed by MRI.

cPET/CT

We performed cPET/CT with an integrated PET/CT scanner; Discovery ST Elite (GE Healthcare, Waukesha, WI, United States). CT parameters were as follows: 120 kVp, 3.75-mm slice thickness, 500-mm transaxial FOV and 512×512 image matrix. PET parameters were as follows: 3.27-mm slice thickness, 700-mm transaxial FOV, 250-mm axial FOV, 128×128 image matrix, and 2.14-mm Gaussian post-reconstruction image filter, and scan duration of 15 minutes. TOF-reconstruction was not available for cPET.

Attenuation correction was performed using CT data. All cPET images were reconstructed with a three-dimensional (3D) ordered subsets expectation-maximization algorithm called VUE Point Plus (4 iterations, 12 subsets, matrix size of 192×192 , voxel size of $3.3 \times 3.3 \times 3.3$ mm, and postfiltering at 2 mm full width at half maximum

(FWHM)). The sensitivity is 8.8 cps/kBq [21].

fxPET/MRI

fxPET

Flexible PET is a mobile PET system based on a SiPM-based DOI TOF detector with MR compatibility [18, 19, 22-25] (Electronic supplementary material 1a). Each of the two-arc detector head consists of 18 detector modules in the transaxial direction and three rings in the axial direction, providing a transaxial FOV of 720 mm and an axial FOV of 150 mm. As fxPET is an external, detachable-type scanner, sufficient FOV of 150 mm can be maintained, while a hybrid PET/MRI with simultaneous acquisition provides a smaller transaxial FOV within the bore of the MR scanner.

Each detector module comprised a scintillation crystal array, light guide, and SiPM array. The scintillation crystal array with arranged light reflectors leads to four-layer DOI encoding. The crystal array for each detector module is made of 16×16 $\text{Lu}_{1.8}\text{Gd}_{0.2}\text{SiO}_5$ (LGSO) crystals, each measuring $2.9 \text{ mm} \times 2.9 \text{ mm} \times 20 \text{ mm}$. The SiPM array was made of 4×4 four-channel customized SiPMs, yielding 64 SiPM channels per block.

The coincidence timing resolution is about 525 ps and the spatial resolution is estimated to be less than 2.5 mm from reconstructed images using an iterative algorithm.

The sensitivity is 2.98 cps/kBq.

Settings for the fxPET/MR system

The fxPET was set in an existing MR unit, in which 1.5-T MR scanner; Excelart Vantage (Canon Medical Systems Cooperation, Otawara, Japan) was equipped (Electronic supplementary material 1b).

We also set an optical camera; Polaris (Northern Digital Inc, Ontario, Canada) in the fxPET/MRI unit. It provided the location of position markers attached to the surface of both modalities, helping better registration.

Data acquisition for fxPET/MRI

All patients moved to the fxPET/MRI unit as soon as possible after cPET/CT. The mean interval between ^{18}F -FDG injection and start of the fxPET was 96 ± 11 min (range, 83-136 min). The interval between cPET and fxPET scan was 34 ± 11 min (range, 21-73 min).

The fxPET scan was performed first, followed by MRI. Using a 12-channel head coil, we acquired MR images: a sagittal 3D magnetization-prepared rapid gradient-echo (MPRAGE) sequence (TR, 9 ms; TE, 4 ms; TI, 1000 ms; matrix size, 256×208 ; resolution, $0.98 \text{ mm} \times 0.98 \text{ mm} \times 0.6 \text{ mm}$; parallel imaging technique, SPEEDER; acceleration factor, 2) and axial T2-weighted 2D TSE sequence (TR, 6000 ms; TE, 80

ms; echo train length, 15; matrix size, 320×256 ; in-plane resolution, $0.92 \text{ mm} \times 0.92 \text{ mm}$; slice thickness, 3 mm; parallel imaging technique, SPEEDER; acceleration factor, 2).

As fxPET is a partial-ring scanner, approximately 30% line-of-responses (LORs) are missed in a PET sinogram space. To reduce degradation of image quality due to incomplete coincidence data, we used TOF information and point-spread functions (PSF) and applied a listmode reconstruction algorithm. All fxPET data were acquired in listmode with the scan duration of 15 minutes and reconstructed using a dynamic row-action maximum-likelihood algorithm (DRAMA) (1 iteration; 128 subsets; matrix size, $480 \times 480 \times 100$; voxel size, $1.5 \times 1.5 \times 1.5 \text{ mm}$; relaxation control parameter, $\beta = 100$ with postfiltering at 5 mm FWHM) [26]. Using the T1WI, we performed a new MRAC method that considers signal attenuation from bone [27] and MR devices (Electronic supplementary material 2). The attenuation map was estimated by a hybrid segmentation-atlas method, which is based on the segmentation of MR image into three regions (bone-air, soft-tissue and water) based on the multi Otsu threshold [28] and the non-rigid spatial transformation of a template attenuation map to assign the template bone and air attenuation values to the patient-specific bone and air regions (i.e., low MR signal regions), respectively [27]. We also performed scatter correction using TOF single scatter

correction [29].

Qualitative evaluation: visual rating

We visually evaluated the image quality of MR and PET images (fxPET and cPET) based on the consensus decisions of two radiologists using a four-point scoring system.

Regarding MR images (T1WI and T2WI), we evaluated overall image quality using the following four-point score: 0 = poor (non-diagnostic quality); 1 = fair (low quality with distinct artifacts and strong noise); 2 = good (satisfactory quality with few artifacts or moderate noise); and 3 = excellent (no artifacts and low noise).

Regarding PET images, we evaluated overall image quality and sharpness considering artifact and noise (Table 1). For 12 patients with intracranial lesions, we examined the number of detected lesions and the subjective contrast of those lesions. We defined lesions as areas showing focal ^{18}F -FDG uptake that was increased or decreased compared with background physiological uptake in the brain.

Quantitative evaluation: registration accuracy and regional ^{18}F -FDG uptake accuracy

For evaluation of registration accuracy and regional ^{18}F -FDG uptake accuracy, we measured the spatial coordinates and regional standardized uptake value (SUV), using

SPM12 (<https://www.fil.ion.ucl.ac.uk/spm/software/spm12>), MATLAB (R2016b, MathWorks, Natick, Massachusetts, United States) and ImageJ software (National Institutes of Health, Bethesda, Maryland, United States).

Quantitative evaluation 1: registration accuracy

CT images were registered to the corresponding cPET images based on the clinical routine, while MR images were registered to the fxPET images using location information obtained from Polaris.

We determined six margins (right, left, anterior, posterior, upper and lower) of physiological ^{18}F -FDG uptake in the brain and measured the spatial coordinates of those six margins. We also determined six margins in the corresponding structural images (CT and T1WI) and measured the spatial coordinates in the same manner. We then calculated coordinate differences between fxPET and T1WI and between cPET and CT for each margin, as an index of misregistration between pair images.

Quantitative evaluation 2: regional ^{18}F -FDG uptake accuracy

PET images and MRI images were registered by rigid registration of SPM12. We performed SUV-based analysis for lesions and normal structures (bilateral caudate nuclei and vermis). Considering the higher soft-tissue contrast of MRI, we used T1WI to create ROI for the lesions, bilateral caudate nuclei and vermis. For the one patient with two

lesions, only the larger lesion was used, so that the following analysis was performed on a per-patient basis. We manually applied ROIs to both fxPET and cPET with manual adjustment by visually checking the ROIs. Then, we measured maximum SUV (SUV_{max}) and mean SUV (SUV_{mean}) within each ROI (Figure 1).

We also performed ROI analysis (SUV_{mean}) for cerebral and cerebellar cortex by using segmentation function of SPM12 as follows: fxPET and cPET images were registered to T1WI, then segmentation was performed for T1WI. Finally, we manually chose the cortices of image slices where the cortices were not affected by intracranial lesions.

Statistics

Visual rating scores of both PET images and the numbers of detected lesions with both PET images were compared using the Wilcoxon signed-rank test. We used the paired t-test to compare coordinate differences between paired images (fxPET/MRI and cPET/CT) and SUV (SUV_{max} and SUV_{mean}) for differences between fxPET and cPET. Pearson's correlation coefficients were calculated to compare SUVs of the fxPET and cPET. A value of $P < 0.05$ was considered statistically significant. Statistical analysis was performed using JMP software (JMP Pro version 14.0; SAS Institute Inc., Cary, United States).

Results

Qualitative evaluation: visual rating of image quality

Representative images of MRI, fxPET, CT, and cPET are shown in Figure 2 and Figure 3.

All images from MRI were of diagnostic quality, with excellent quality in 19 patients and good quality in two patients.

Table 2 shows the visual rating results for PET images. All fxPET images were also of diagnostic quality, although image quality was significantly lower for fxPET than for cPET ($P < 0.001$). The number of detected lesions was 12 in fxPET and 13 in cPET, showing no significant difference. The one lesion was not detected in fxPET due to small size and low FDG uptake.

Quantitative evaluation 1: registration accuracy

Mean misregistration of fxPET/MRI and cPET/CT in the six margins is shown in Table 3. Although mean misregistration of fxPET/MRI were significantly larger than those of cPET/CT in the left (1.35 ± 0.22 mm, 0.64 ± 0.13 mm, $P = 0.01$), anterior (2.00 ± 0.20 mm, 1.19 ± 0.26 mm, $P = 0.01$) and superior (2.87 ± 0.40 mm, 1.43 ± 0.22 mm, $P = 0.004$) margins, no significant differences were seen for the right, posterior and inferior

margins.

Quantitative evaluation 2: regional ^{18}F -FDG uptake accuracy

The results of SUV analysis are shown in Table 4. In the lesions, SUVmax and SUVmean of fxPET (8.46 ± 3.12 and 5.11 ± 2.21 , respectively) were significantly higher than those of cPET (5.81 ± 2.62 and 3.33 ± 1.73 , respectively) ($P < 0.001$). We showed a high correlation between fxPET and cPET for both SUVmax ($R = 0.84$, $P < 0.001$) and SUVmean ($R = 0.79$, $P = 0.002$) in the lesions (Figure 4).

SUVmax and SUVmean of the fxPET were significantly higher than those of cPET in normal structures (bilateral caudate nuclei and vermis). We showed high correlation between the fxPET and cPET for both SUVmax ($R = 0.85$, 0.87 ; $P < 0.001$, $P < 0.001$, respectively) and SUVmean ($R = 0.83$, 0.87 ; $P < 0.001$, $P < 0.001$, respectively) in bilateral caudate nuclei (Figure 5a, b) and a moderate correlation between fxPET and cPET for both SUVmax ($R = 0.65$, $P = 0.002$) and SUVmean ($R = 0.63$, $P = 0.002$) in the vermis (Figure 5c, d).

SUVmean of the fxPET was also significantly higher than that of cPET in the segmented cerebral and cerebellar cortex (Figure 5e, f). We found high correlation between the fxPET and cPET for SUVmean in cerebral cortex ($R = 0.88$, $P < 0.001$), and moderate correlation in cerebellar cortex ($R = 0.51$, $P = 0.019$).

Multiple slices including cerebellum were shown for better understanding fxPET and cPET are also shown in Figure 6.

Discussion

We evaluated clinical feasibility of a sequential fxPET/MRI system using a newly developed mobile PET, compared with cPET/CT for brain imaging. The image quality from fxPET/MRI was within the diagnostic range, showing the comparable lesion detectability to cPET. Misregistration from fxPET/MRI was below 3mm. SUVs of fxPET showed a high correlation with those of cPET. We consider that these results confirmed the clinical feasibility of fxPET/MRI.

All MR images showed excellent or good image quality. This confirms that setting the fxPET in the MR unit did not cause critical degradation of MR images, thereby demonstrating the MR-compatibility of fxPET. All fxPET images were also of diagnostic quality, although image quality was significantly lower than that of cPET images.

Mean misregistration of fxPET/MRI was below 3 mm in all margins, comparable to the result of a prior phantom study (around 2 mm) [25]. Location information from optical camera reflecting head position change was used for better registration and conventional rigid body transformation has also been effective for registration of brain

images [30]. Although misregistration was significantly higher for sequentially acquired PET/MRI than for PET/CT or simultaneously acquired PET/MRI in previous studies [20, 31], our results showed comparable registration accuracy for fxPET/MRI, irrespective of sequential acquisition. The registration of fxPET/MRI was mainly dependent on the registration accuracy of Polaris system. There is no previous study of brain PET with Polaris system with detailed measurement of registration as this study. The retrospective registration correction should be developed to achieve improvement of registration accuracy.

The possible factors for fxPET image quality and registration accuracy include incomplete data acquisition (due to the open ring form) and attenuation correction methods. For reducing image degradation due to incomplete data, we used TOF, as this method had been suggested as effective in limited angle PET scanner as far as maintaining appropriate timing resolution corresponding to the angular coverage [32]. We also used PSF because it increased the SUV of small lesions by improving spatial resolution [33]. However, considering that reconstructed images using PSF were suggested to be deformed on incomplete data acquisition, application of image-based modeling could be better [34]. For attenuation correction, we performed MRAC. Misregistration between PET and MR images would interfere with application of the attenuation map, causing

inaccurate MRAC. Skull bones and artificial devices such as MR coils and table affect the attenuation map [35-37], therefore, we took into account attenuation induced by bones, MR coils and table to avoid SUV underestimation [38-43]. Also, TOF reconstruction has been suggested to reduce artifacts and improve the quantitative accuracy of MRAC [44, 45]. MR-AC_SEG BONE, which was similar to our MRAC method, demonstrated promising results, and performs well within 5 % CTAC reference. The current study focused on the clinical feasibility of fxPET/MRI, and further studies required to compare our MRAC method and other MRAC methods [46].

SUV_{max} and SUV_{mean} showed high correlation between fxPET and cPET, meaning that fxPET successfully determined both physiological ¹⁸F-FDG uptake of normal structures and abnormal ¹⁸F-FDG uptake of lesions. Although SUVs (SUV_{max} and SUV_{mean}) of fxPET and cPET showed a high correlation, SUVs of fxPET were significantly higher than those of cPET. We attribute the difference in SUVs between fxPET and cPET to spatial resolution and attenuation correction. The spatial resolution of fxPET was estimated to be less than 2.5 mm, higher than that of cPET (less than 6 mm). As high spatial resolution reduces partial volume effects, this would affect SUVs. Although our MRAC method took attenuation of bones, MR coil and table into consideration, measurement error associated with the attenuation coefficient of template

attenuation map, MR coil and table can occur, and other structures (such as fixation devices and metallic implants) can influence signal attenuation.

Our study has several limitations that should be considered. First, relatively small number of patients were enrolled in this study ($n = 21$), and only 12 patients had visible intracranial lesions. It seems better to enroll a larger number of patients especially with various types of visible intracranial lesions. Second, 1.5-T MRI scanner was used in our study. A 3-T MRI with better SNR could achieve more accurate ROI definition in T1WI. However, the strong magnetic field might cause severe artifacts in PET images, especially when lesions are located near air cavities and high-energy positrons are used [47]. We should take such artifacts into account when combining fxPET with a 3-T MR unit. Third, PSF correction was used for image reconstruction for fxPET (DRAMA), on the contrary, PSF correction was not used for cPET (VUE Point Plus). PSF correction increased cortices uptake compared with image reconstruction without PSF correction [48]. In addition, recent digital PET/CT system with PSF correction showed higher SUVmax than analog PET/CT system without PSF correction [49]. Thus, higher SUVs of fxPET may attribute to PSF correction adapted in DRAMA. Fourth, the scan timing of FDG injection is different between fxPET and cPET, which also affected the image quality because FDG distribution changes according to the time after the tracer injection.

Fifth, since we evaluated the registration accuracy manually, the voxel resolution or post gaussian filtering may have affected the results. Sixth, the differences of regional FDG uptake of fxPET and cPET were large in supratentorial regions (caudate, cerebral cortex) and small in infratentorial regions (vermis, cerebellar cortex). MRAC at skull base was more difficult than that at the skull convexity. MRAC and PSF correction affected SUV, which should be further investigated. Lastly, fxPET was installed to the different room from cPET/CT in this study. The interval between cPET and fxPET was mainly due to the transfer from cPET/CT room to fxPET/MRI room.

For future work, we would like to focus on the flexibility of fxPET, which is one of the most unique features of this system compared to integrated PET/MR. MR insertable brain PET was reported to be beneficial for simultaneous PET and MR imaging of the human brain [50], however, body PET scan is probably difficult due to the limited FOV. Brain PET and body PET are available at our fxPET/MRI system. The dual-head configuration of the fxPET enables flexible positioning on image acquisition. Closer positioning of the two-arc detector head to the target would increase the count, leading to potential improvements in image quality, which has been already demonstrated in body fxPET/CT imaging [51]. Closer positioning also reduces image quality degradation associated with incomplete coincident data acquisition due to the open ring form [51].

Combination of fxPET with an existing MRI scanner and sequential acquisition of fxPET and MRI is mandatory, however, less expensive cost and no additional space for integrated PET/MRI system are advantages for fxPET. Improvement of image quality of fxPET should be necessary to establish the modality of mobile PET with MR-compatibility. MR compatibility at 3-T MR scanner is one of the important issues for PET/MRI. We currently conduct fxPET/MRI study at 3-T MR scanner at our institute.

Conclusion

The fxPET/MRI system showed image quality within the diagnostic range, registration accuracy below 3mm and regional ^{18}F -FDG uptake highly correlated with that of cPET/CT.. We thus consider that this study confirmed the clinical feasibility of fxPET/MRI.

Disclosure of Conflicts of Interest

Dr. Kaori Togashi received a research grant from Shimadzu Corporation. The other authors declare that they have no conflicts of interest.

References

1. Bar-Shalom R, Yefremov N, Guralnik L, Gaitini D, Frenkel A, Kuten A, et al. Clinical performance of PET/CT in evaluation of cancer: additional value for diagnostic imaging and patient management. *J Nucl Med.* 2003;44(8):1200-9.
2. Antoch G, Saoudi N, Kuehl H, Dahmen G, Mueller SP, Beyer T, et al. Accuracy of whole-body dual-modality fluorine-18-2-fluoro-2-deoxy-D-glucose positron emission tomography and computed tomography (FDG-PET/CT) for tumor staging in solid tumors: comparison with CT and PET. *J Clin Oncol.* 2004;22(21):4357-68.
3. Scarfone C, Lavelly WC, Cmelak AJ, Delbeke D, Martin WH, Billheimer D, et al. Prospective feasibility trial of radiotherapy target definition for head and neck cancer using 3-dimensional PET and CT imaging. *J Nucl Med.* 2004;45(4):543-52.
4. Shimizu Y, Kudo K, Kameda H, Harada T, Fujima N, Toyonaga T, et al. Prediction of Hypoxia in Brain Tumors Using a Multivariate Model Built from MR Imaging and (18)F-Fluorodeoxyglucose Accumulation Data. *Magn Reson Med Sci.* 2020;19(3):227-34.
5. Matsuda H, Shigemoto Y, Sato N. Neuroimaging of Alzheimer's disease: focus on amyloid and tau PET. *Japanese journal of radiology.* 2019;37(11):735-49.
6. Schiepers C, Dahlbom M. Molecular imaging in oncology: the acceptance of

PET/CT and the emergence of MR/PET imaging. *Eur Radiol.* 2011;21(3):548-54.

7. Loeffelbein DJ, Souvatzoglou M, Wankerl V, Martinez-Moller A, Dinges J, Schwaiger M, et al. PET-MRI fusion in head-and-neck oncology: current status and implications for hybrid PET/MRI. *J Oral Maxillofac Surg.* 2012;70(2):473-83.

8. von Schulthess GK, Schlemmer HP. A look ahead: PET/MR versus PET/CT. *Eur J Nucl Med Mol Imaging.* 2009;36 Suppl 1:S3-9.

9. Antoch G, Vogt FM, Freudenberg LS, Nazaradeh F, Goehde SC, Barkhausen J, et al. Whole-body dual-modality PET/CT and whole-body MRI for tumor staging in oncology. *Jama.* 2003;290(24):3199-206.

10. Drzezga A, Souvatzoglou M, Eiber M, Beer AJ, Furst S, Martinez-Moller A, et al. First clinical experience with integrated whole-body PET/MR: comparison to PET/CT in patients with oncologic diagnoses. *J Nucl Med.* 2012;53(6):845-55.

11. Krumm P, Mangold S, Gatidis S, Nikolaou K, Nensa F, Bamberg F, et al. Clinical use of cardiac PET/MRI: current state-of-the-art and potential future applications. *Japanese journal of radiology.* 2018;36(5):313-23.

12. Al-Nabhani KZ, Syed R, Michopoulou S, Alkalbani J, Afaq A, Panagiotidis E, et al. Qualitative and quantitative comparison of PET/CT and PET/MR imaging in clinical practice. *J Nucl Med.* 2014;55(1):88-94.

13. Garibotto V, Heinzer S, Vulliemoz S, Guignard R, Wissmeyer M, Seeck M, et al. Clinical applications of hybrid PET/MRI in neuroimaging. *Clin Nucl Med.* 2013;38(1):e13-8.
14. Catana C, Drzezga A, Heiss WD, Rosen BR. PET/MRI for neurologic applications. *J Nucl Med.* 2012;53(12):1916-25.
15. Kishi S, Maeda M, Kogue R, Umino M, Matsubara T, Sakuma H. Hemangioblastoma of the Cerebellopontine Angle Evaluated with Pseudocontinuous Arterial Spin Labeling. *Magn Reson Med Sci.* 2020.
16. Imaizumi A, Obata T, Kershaw J, Tachibana Y, Inubushi M, Koizumi M, et al. Imaging of Hypoxic Tumor: Correlation between Diffusion-weighted MR Imaging and (18)F-fluoroazomycin Arabinoside Positron Emission Tomography in Head and Neck Carcinoma. *Magn Reson Med Sci.* 2020;19(3):276-81.
17. Akram MSH, Obata T, Yamaya T. Microstrip Transmission Line RF Coil for a PET/MRI Insert. *Magn Reson Med Sci.* 2020;19(2):147-53.
18. Yamakawa Y, Kobayashi T, Furuta M, Sato M, Ohi J, Tonami H, et al., editors. Development of a dual-head mobile DOI-TOF PET system having multi-modality compatibility. Nuclear Science Symposium and Medical Imaging Conference (NSS/MIC), 2014 IEEE; 2014: IEEE.

19. Furumiya T, Tsuda T, Tonami H, Satoh M, Nakazawa M, Ohi J, et al., editors. Development of a SiPM based MR-compatible DOI-TOF-PET detector. Nuclear Science Symposium and Medical Imaging Conference (NSS/MIC), 2014 IEEE; 2014: IEEE.
20. Brendle CB, Schmidt H, Fleischer S, Braeuning UH, Pfannenber CA, Schwenger NF. Simultaneously acquired MR/PET images compared with sequential MR/PET and PET/CT: alignment quality. *Radiology*. 2013;268(1):190-9.
21. Teras M, Tolvanen T, Johansson JJ, Williams JJ, Knuuti J. Performance of the new generation of whole-body PET/CT scanners: Discovery STE and Discovery VCT. *Eur J Nucl Med Mol Imaging*. 2007;34(10):1683-92.
22. Kobayashi T, Kitamura K, editors. Design considerations for a partial-ring, multi-modal compatible whole-body TOF PET scanner: Flexible PET. Nuclear Science Symposium and Medical Imaging Conference (NSS/MIC), 2012 IEEE; 2012: IEEE.
23. Nakazawa M, Ohi J, Furumiya T, Tsuda T, Furuta M, Sato M, et al., editors. PET data acquisition (DAQ) system having scalability for the number of detector. Nuclear Science Symposium and Medical Imaging Conference (NSS/MIC), 2012 IEEE; 2012: IEEE.
24. Furuta M, Satoh M, Ohi J, Tonami H, Furumiya T, Tsuda T, et al., editors. Development of a proof of concept system for multi-modal compatible PET: Flexible PET.

Nuclear Science Symposium and Medical Imaging Conference (NSS/MIC), 2013 IEEE; 2013: IEEE.

25. Nakamoto R, Nakamoto Y, Ishimori T, Fushimi Y, Kido A, Togashi K. Comparison of PET/CT with Sequential PET/MRI Using an MR-Compatible Mobile PET System. *J Nucl Med.* 2018;59(5):846-51.

26. Nakayama T, Kudo H, editors. Derivation and implementation of ordered-subsets algorithms for list-mode PET data. Nuclear Science Symposium Conference Record, 2005 IEEE; 2005: IEEE.

27. Tanigawa A, Yamaya T, Kawaguchi H, Hirano Y, Shiraishi T, Tanimoto K, et al., editors. Hybrid segmentation-atlas method for PET-MRI attenuation correction. Nuclear Science Symposium and Medical Imaging Conference (NSS/MIC), 2012 IEEE; 2012: IEEE.

28. Liao PS, Chen TS, Chung PC. A fast algorithm for multilevel thresholding. *Journal of Information Science and Engineering.* 2001;17(5):713-27.

29. Watson C. Extension of single scatter simulation to scatter correction of time-of-flight PET. *IEEE Transactions on Nuclear Science.* 2007;54(5):1679-86.

30. Roy P, Lee JK, Sheikh A, Lin W. Quantitative Comparison of Misregistration in Abdominal and Pelvic Organs Between PET/MRI and PET/CT: Effect of Mode of

Acquisition and Type of Sequence on Different Organs. *AJR Am J Roentgenol.* 2015;205(6):1295-305.

31. Huang S-y, Savic D, Yang J, Shrestha U, Seo Y, editors. The effect of magnetic field on positron range and spatial resolution in an integrated whole-body time-of-flight PET/MRI system. *IEEE Nuclear Science Symposium conference record Nuclear Science Symposium*; 2014: NIH Public Access.

32. Surti S, Karp JS. Design considerations for a limited angle, dedicated breast, TOF PET scanner. *Phys Med Biol.* 2008;53(11):2911-21.

33. Shang K, Cui B, Ma J, Shuai D, Liang Z, Jansen F, et al. Clinical evaluation of whole-body oncologic PET with time-of-flight and point-spread function for the hybrid PET/MR system. *Eur J Radiol.* 2017;93:70-5.

34. Matej S, Li Y, Panetta J, Karp JS, Surti S. Image-based modeling of PSF deformation with application to limited angle PET data. *IEEE transactions on nuclear science.* 2016;63(5):2599-606.

35. Martinez-Moller A, Souvatzoglou M, Delso G, Bundschuh RA, Chefd'hotel C, Ziegler SI, et al. Tissue classification as a potential approach for attenuation correction in whole-body PET/MRI: evaluation with PET/CT data. *J Nucl Med.* 2009;50(4):520-6.

36. Wagenknecht G, Kaiser HJ, Mottaghy FM, Herzog H. MRI for attenuation

correction in PET: methods and challenges. *Magma*. 2013;26(1):99-113.

37. Martinez-Moller A, Nekolla SG. Attenuation correction for PET/MR: problems, novel approaches and practical solutions. *Z Med Phys*. 2012;22(4):299-310.

38. Aznar MC, Sersar R, Saabye J, Ladefoged CN, Andersen FL, Rasmussen JH, et al. Whole-body PET/MRI: the effect of bone attenuation during MR-based attenuation correction in oncology imaging. *Eur J Radiol*. 2014;83(7):1177-83.

39. Akbarzadeh A, Ay MR, Ahmadian A, Alam NR, Zaidi H. MRI-guided attenuation correction in whole-body PET/MR: assessment of the effect of bone attenuation. *Ann Nucl Med*. 2013;27(2):152-62.

40. Samarin A, Burger C, Wollenweber SD, Crook DW, Burger IA, Schmid DT, et al. PET/MR imaging of bone lesions--implications for PET quantification from imperfect attenuation correction. *Eur J Nucl Med Mol Imaging*. 2012;39(7):1154-60.

41. Catana C, van der Kouwe A, Benner T, Michel CJ, Hamm M, Fenchel M, et al. Toward implementing an MRI-based PET attenuation-correction method for neurologic studies on the MR-PET brain prototype. *J Nucl Med*. 2010;51(9):1431-8.

42. Delso G, Martinez-Moller A, Bundschuh RA, Ladebeck R, Candidus Y, Faul D, et al. Evaluation of the attenuation properties of MR equipment for its use in a whole-body PET/MR scanner. *Phys Med Biol*. 2010;55(15):4361-74.

43. MacDonald LR, Kohlmyer S, Liu C, Lewellen TK, Kinahan PE. Effects of MR surface coils on PET quantification. *Med Phys*. 2011;38(6):2948-56.
44. Mehranian A, Zaidi H. Impact of time-of-flight PET on quantification errors in MR imaging-based attenuation correction. *J Nucl Med*. 2015;56(4):635-41.
45. Mehranian A, Arabi H, Zaidi H. Quantitative analysis of MRI-guided attenuation correction techniques in time-of-flight brain PET/MRI. *Neuroimage*. 2016;130:123-33.
46. Ladefoged CN, Law I, Anazodo U, St Lawrence K, Izquierdo-Garcia D, Catana C, et al. A multi-centre evaluation of eleven clinically feasible brain PET/MRI attenuation correction techniques using a large cohort of patients. *Neuroimage*. 2017;147:346-59.
47. Kolb A, Sauter AW, Eriksson L, Vandenbrouke A, Liu CC, Levin C, et al. Shine-Through in PET/MR Imaging: Effects of the Magnetic Field on Positron Range and Subsequent Image Artifacts. *J Nucl Med*. 2015;56(6):951-4.
48. Salvadori J, Imbert L, Perrin M, Karcher G, Lamiral Z, Marie PY, et al. Head-to-head comparison of image quality between brain (18)F-FDG images recorded with a fully digital versus a last-generation analog PET camera. *EJNMMI Res*. 2019;9(1):61.
49. Fuentes-Ocampo F, Lopez-Mora DA, Flotats A, Paillahueque G, Camacho V, Duch J, et al. Digital vs. analog PET/CT: intra-subject comparison of the SUVmax in target lesions and reference regions. *Eur J Nucl Med Mol Imaging*. 2019;46(8):1745-50.

50. Hong KJ, Choi Y, Jung JH, Kang J, Hu W, Lim HK, et al. A prototype MR insertable brain PET using tileable GAPD arrays. *Med Phys.* 2013;40(4):042503.
51. Watanabe M, Nakamoto Y, Nakamoto R, Ishimori T, Saga T, Togashi K. Performance Evaluation of a Newly Developed MR-Compatible Mobile PET Scanner with Two Detector Layouts. *Mol Imaging Biol.* 2019.

FIGURE LEGENDS

Figure 1.

Representative images of MR (a, d, g), fxPET (b, e, h) and cPET (c, f, i) with a brain tumor (glioblastoma) are shown. The ROIs of the lesion (a, b, c), the caudate nuclei (d, e, f), and the vermis (g, h, i) are shown.

Figure 2.

Representative images of a case of glioblastoma. T1-weighted image (a), fxPET (b), CT (c), cPET (d), % difference in absolute values (e), and MRAC of fxPET (f) are shown. Both PET images show regional FDG uptake is increased in the tumor (arrow). Note that there was a metallic artifact associated with extracranial metal (arrowhead) on T1WI (a), CT image (c), and MRAC image (f). The effect of metallic artifact is limited on MRAC.

Figure 3.

Representative images of a case of meningioma. T1-weighted image (a), fxPET (b), CT (c), cPET (d) and % difference in absolute values (e) are shown. Both PET images show regional FDG uptake is decreased in the lateral side to the right temporal lobe (arrow).

Figure 4.

Regional FDG uptake of fxPET and cPET in lesions (n=12). (a) SUVmax, (b) SUVmean in lesions. Both SUVmax ($R = 0.84$, $P < 0.001$) and SUVmean ($R = 0.79$, $P = 0.002$) show high linear correlations between fxPET and cPET. Equation of linear regression lines are shown as follows. (a) Lesion, SUVmax, cPET = $-0.18 + 0.71 \times \text{fxPET}$; (b) Lesion, SUVmean, cPET = $0.18 + 0.62 \times \text{fxPET}$.

Figure 5.

Regional FDG uptake of fxPET and cPET in bilateral caudate nuclei (a, b), vermis (c, d), and segmented cerebral (e) and cerebellar cortex (f). We showed high correlation between the fxPET and cPET for both SUVmax ($R = 0.85, 0.87$; $P < 0.001, P < 0.001$, respectively) and SUVmean ($R = 0.83, 0.87$; $P < 0.001, P < 0.001$, respectively) in bilateral caudate nuclei (a, b). Equation of linear regression lines are shown as follows. (a) Rt. Caudate, SUVmax, cPET = $1.01 + 0.68 \times \text{fxPET}$ Lt. Caudate, SUVmax, cPET = $0.90 + 0.73 \times \text{fxPET}$. (b) Rt. Caudate, SUVmean, cPET = $0.68 + 0.67 \times \text{fxPET}$ Lt. Caudate, SUVmean, cPET = $0.27 + 0.76 \times \text{fxPET}$. We showed a moderate correlation between fxPET and cPET for both SUVmax ($R = 0.65$, $P = 0.002$) and SUVmean ($R =$

0.63, $P = 0.002$) in the vermis (c, d). Equation of linear regression lines are shown as follows. (c) Vermis, SUVmax, cPET = $2.21 + 0.67 \times \text{fxPET}$; (d) Vermis, SUVmean, cPET = $2.64 + 0.58 \times \text{fxPET}$. We found high correlation between the fxPET and cPET for SUVmean in cerebral cortex ($R = 0.88$, $P < 0.001$) (e), and moderate correlation in cerebellar cortex ($R = 0.51$, $P = 0.019$) (f). Equation of linear regression lines are shown as follows. (e) Cerebral Cortex, SUVmean, cPET = $0.41 + 0.69 \times \text{fxPET}$; (f) Cerebellar Cortex, SUVmean, cPET = $1.51 + 0.60 \times \text{fxPET}$.

Figure 6.

Multiple slices including cerebellum were shown for better understanding fxPET and cPET of the images described in Figure 2 (a, b, c, d and e) and Figure 3 (f, g, h, i and j). T1-weighted image (a, f), fxPET (b, g), CT (c, h), cPET (d, i) and % difference in absolute values (e, j) are shown.

Electronic supplementary material 1.

Flexible PET/MRI. (a) Flexible PET (fxPET), a newly developed mobile PET system with MR-compatibility. (b) The fxPET/MRI system, achieved by setting fxPET in an existing MR unit.

Electronic supplementary material 2.

The attenuation map was estimated by a hybrid segmentation-atlas method, which is based on the segmentation of MR image into three regions (bone-air, soft-tissue and water) and the non-rigid spatial transformation of a template attenuation map to assign the template bone and air attenuation values to the patient-specific bone and air regions, respectively.

Figure 1

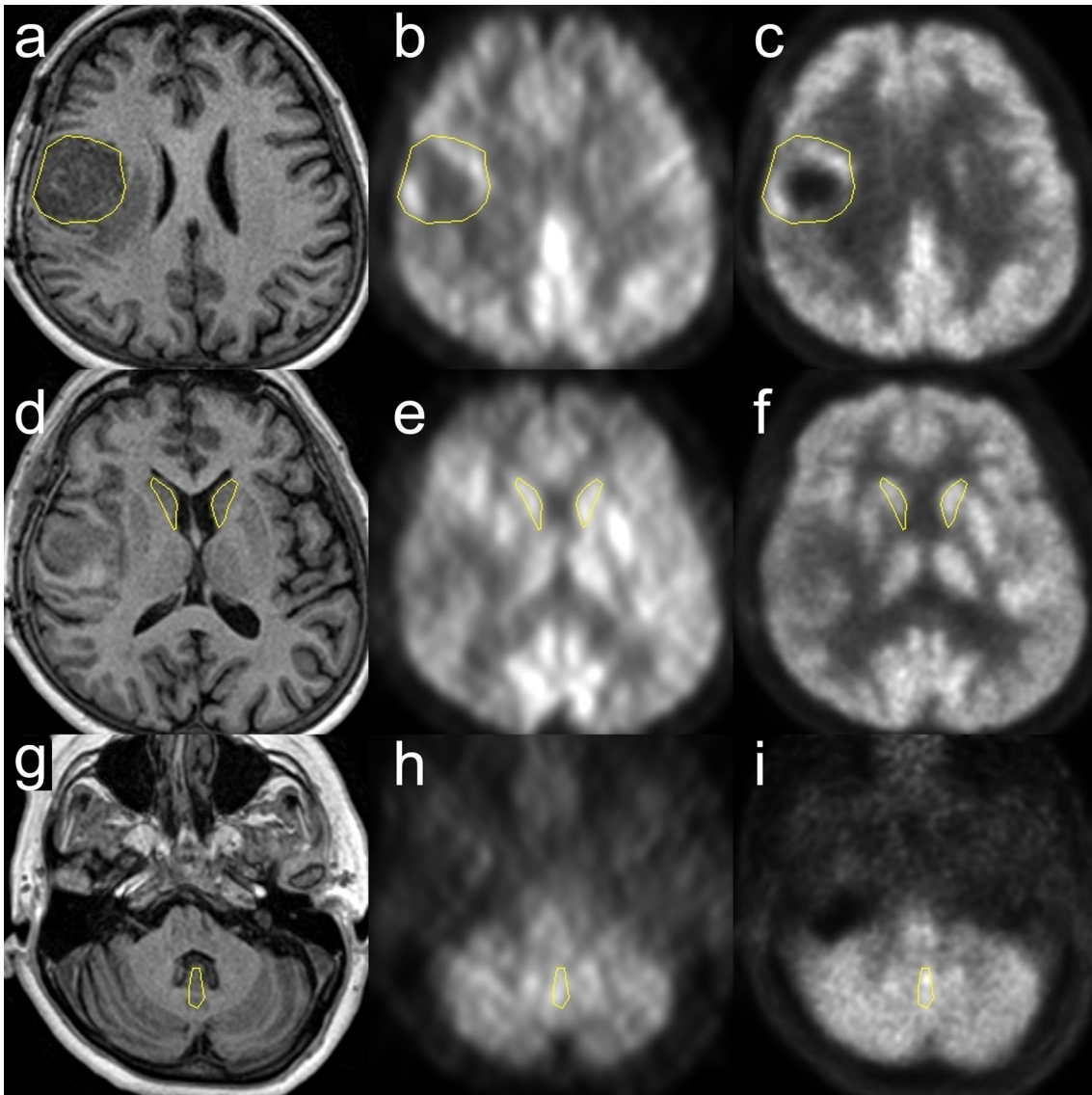


Figure 2

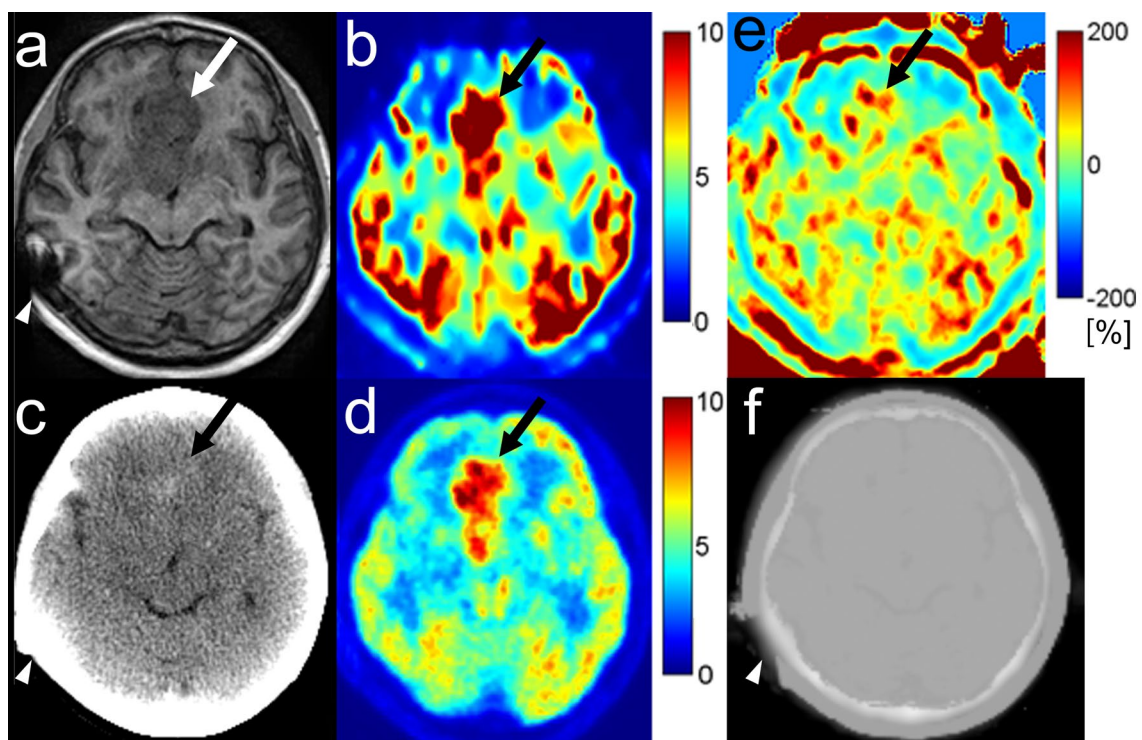


Figure 3

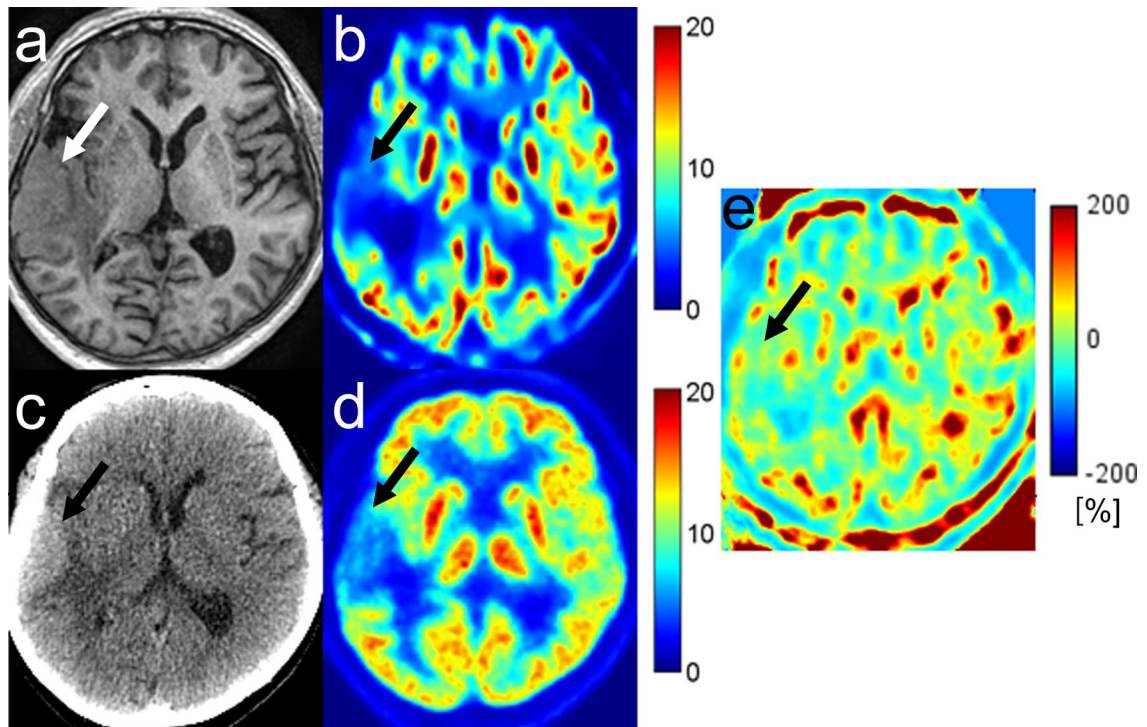


Figure 4

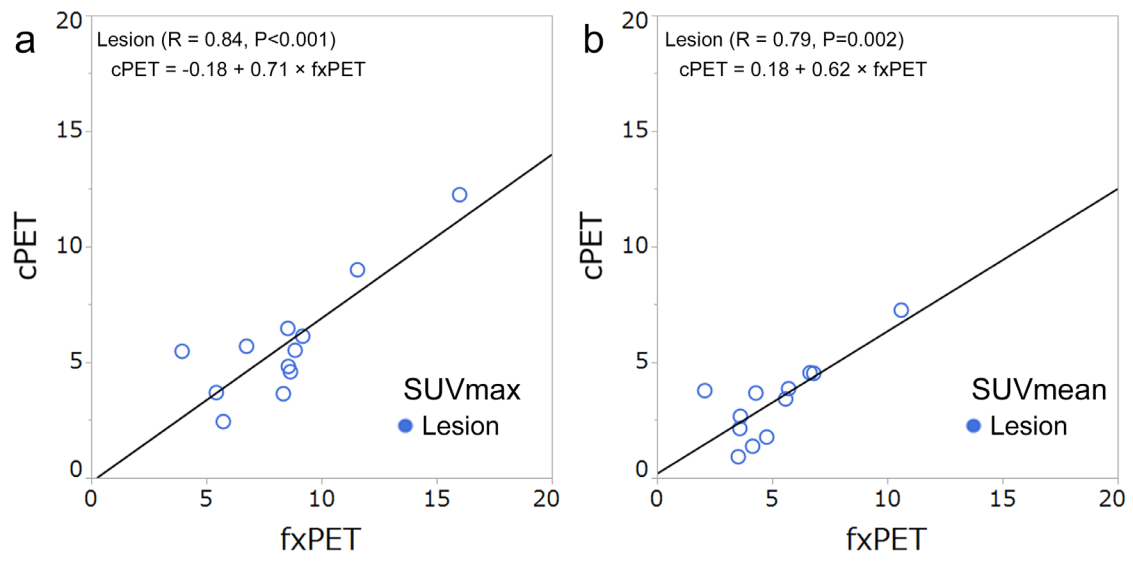


Figure 5

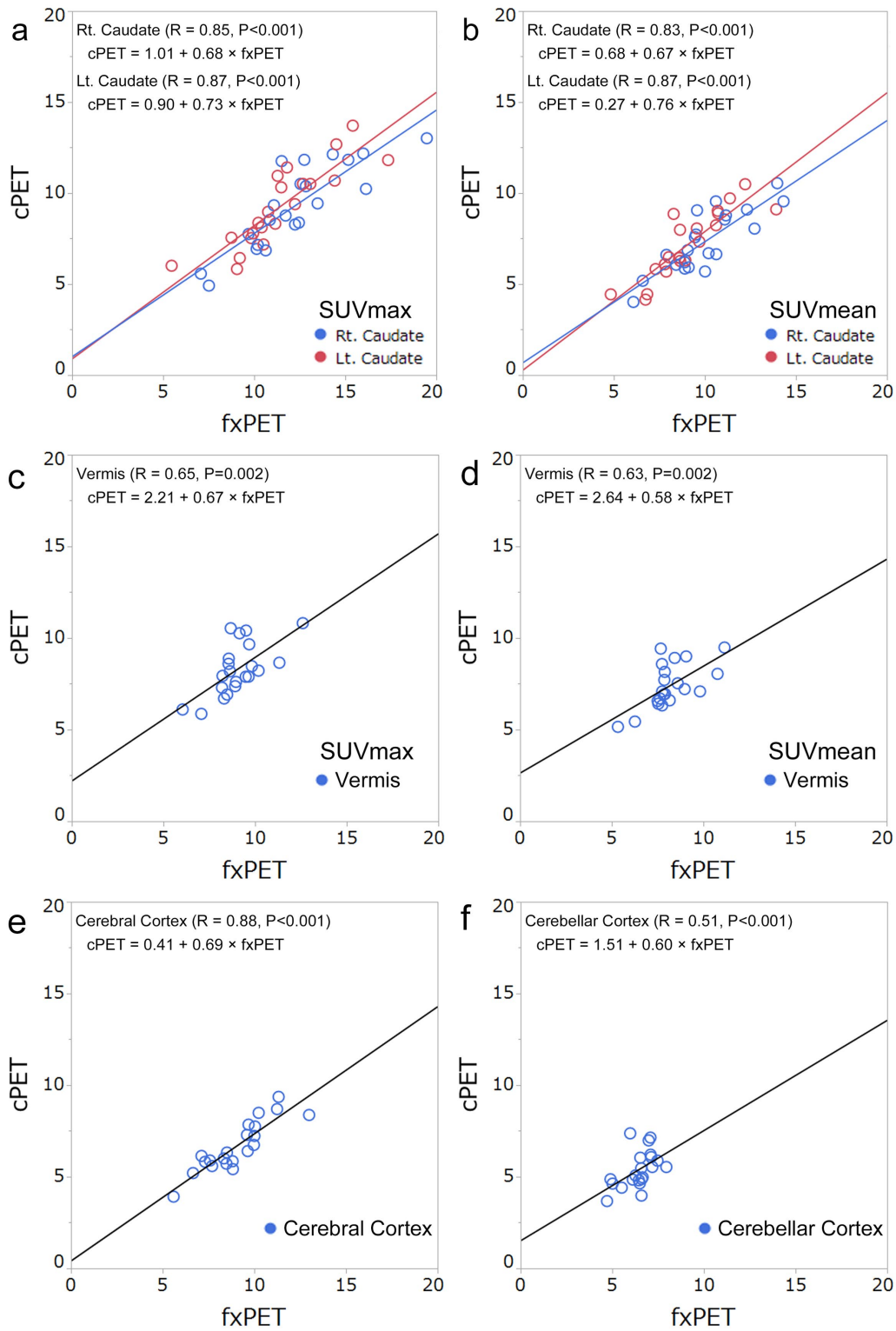


Figure 6

